Chemical Engineering Journal 493 (2024) 152485

Contents lists available at ScienceDirect

Chemical Engineering Journal

journal homepage: www.elsevier.com/locate/cej

Site-selective Mg-doping regulated charge storage in $NaFe_2PO_4(SO_4)_2$ for high energy sodium-ion batteries

Sharad Dnyanu Pinjari [a], Ravi C. Dutta [b,c], Shuimei Chen [d], Purandas Mudavath [a], Xiaodan Huang [d], John Bell [e], Suresh K. Bhatia [c], Ashok Kumar Nanjundan [e,*], Rohit Ranganathan Gaddam [a,*]

[a] Department of Chemical Engineering, Indian Institute of Science Education and Research-Bhopal, Madhya Pradesh 562066, India
[b] Department of Chemical Engineering, Indian Institute of Technology Dharwad, Karnataka,580011, India
[c] School of Chemical Engineering, The University of Queensland, Brisbane, QLD 4072, Australia
[d] Australian Institute for Bioengineering and Nanotechnology, The University of Queensland, Brisbane 4072, Australia
[e] Centre for Future Materials and the School of Engineering, University of Southern Queensland, QLD 00244B, Australia

ARTICLE INFO

Keywords:
Sodium-ion battery
Density functional theory
Cathodes
NASICON
Chemomechanical synthesis

ABSTRACT

The absence of compatible cathodes with higher specific capacity and energy density hampers the full-scale commercial adaptation of sodium-ion batteries (NIB). Engineering NASICON cathodes with Fe redox centre and mixed polyanions is promising to overcome the bottlenecks. Our study uses a chemo-mechanical route to synthesise $NaFe_{2-x}Mg_xPO_4(SO_4)_2$ (NFMPS), where the dopant, Mg, is strategically positioned at the Fe sites. To our knowledge, such a chemo-mechanical synthesis of NASICON-type metal-phosphosulphate has not been attempted so far. Our work presents Mg^{2+} doping at the Fe site, in particular, for a NASICON-type $NaFe_2PO_4(SO_4)_2$ for the first time. With varying dopant concentrations, NFMPS is optimised to show a remarkable reversible capacity of around 111 mAh g^{-1} at C/20 with a corresponding energy density of 324 Wh kg^{-1}. Even after 100 cycles at a C/5 current rate, the material retains 86.45 % of its initial capacity. An in-depth analysis of sodium-ion storage in NFMPS was conducted using electrochemical investigation, ex-situ characterisation methods and DFT calculations, where the presence of mixed polyanion and the dopant seem to enhance reversible sodium-ion (de)intercalation synergistically. DFT calculations indicate that the presence of Mg^{2+} can affect the localised electronic state of NFMPS and reduce the energy band gap of the material as evidenced from the electrical conductivity measurements for NFMPS. Ex-situ XRD studies at various (de)sodiation states showed that Mg-doping helps in retaining the material's structural integrity and providing larger lattice sites for enhanced sodium-ion diffusion (ranging from 10^{-11} to 10^{-12} cm^2 s^{-1}). Higher working voltages, better sodium-ion transport, and capacity retention make NFMPS a promising candidate as a sodium-ion battery cathode.

1. Introduction

Decades of excessive reliance on non-renewable energy sources, contributing to the onset of climate change, have raised grave environmental concerns [1–4]. Consequently, pursuing energy-generation technologies with a low "carbon footprint", such as solar, wind, and hydropower, has gained substantial traction [5]. However, despite the increased use of renewable energy, the discrepancy in energy production and utilization due to intermittency demonstrates the urgent need for energy storage technologies.

Batteries, particularly lithium-ion batteries (LIB), represent a facile energy storage technology with an upright balance between energy and power density, making it an ideal choice for stationary and non-stationary applications [6–11]. However, the resource scarcity of lithium will lead to increased costs and geopolitical tensions [12]. Research on alternative battery technologies is on the rise to address these challenges. Amongst all other technologies, sodium-ion batteries (NIBs) have garnered significant attention given the practically unlimited resource availability and comparable (electro)chemical characteristics with lithium [13,14]. However, the larger ionic radius of sodium (1.02 Å for Na^+ *vs.* 0.76 Å for Li^+) hampers the efficient diffusion of sodium ions, rendering the electrodes designed for LIBs unsuitable for

* Corresponding authors.
E-mail addresses: ashok.nanjundan@unisq.edu.au (A.K. Nanjundan), rohitg@iiserb.ac.in (R.R. Gaddam).

https://doi.org/10.1016/j.cej.2024.152485
Received 20 January 2024; Received in revised form 3 May 2024; Accepted 21 May 2024
Available online 23 May 2024

NIBs [15,16]. While anodes like hard carbons show better sodium-ion uptake, [17] the unavailability of promising cathodes with good performance and structural integrity remains a significant obstacle to the widespread adoption of NIBs.

Cathodes with 3D pathways that provide large interstitial space for facile sodium-ion diffusion can enhance the overall energy density of NIBs. In this regard, polyanion compounds, especially Natrium Super Ionic Conductors (NASICONs), are considered promising cathodes for Na-ion storage [18–20]. NASICONs have a general formula, $A_xMM'(XO_4)_3$, where A represents alkali-metal ions (with $0 \leq x \leq 5$), and M/M' denote multivalent cations such as Fe^{2+}, Cr^{3+}, Mg^{2+}, V^{3+}, Nb^{5+}, Ti^{4+} etc., while X can stand for elements like P, Si, and S [21]. Most NASICON-related cathode research focuses on using vanadium as the multivalent cation paired with phosphate as the polyanion. Despite its favourable electrochemical properties, vanadium phosphate faces challenges due to material toxicity and the high cost of vanadium precursors, which limit its scalability [22]. Therefore, an alternative, low-cost, earth-abundant, non-toxic transition metal, such as iron, can be considered a viable multivalent cation.

The performance of Fe-based NASICONs can be further improved by the synergistic effects arising from utilising multiple polyanions. For instance, in the case of sodium iron phosphate, substituting a portion of the $[PO_4]^{3-}$ polyanions with highly electronegative $[SO_4]^{2-}$ polyanions can notably elevate the redox potential of M^n/M^{n+} (*vs.* Na/Na^+) due to the inductive effects of $[SO_4]^{2-}$ [23–25]. However, it is important to note that while partial substitution is advantageous, completely replacing $[PO_4]^{3-}$ with $[SO_4]^{2-}$ is unfavourable due to the higher molar mass of sulphate ($[SO_4]^{2-}$) compared to phosphate ($[PO_4]^{3-}$) (i.e., 96.06 g mol^{-1} for sulphate *vs.* 94.97 g mol^{-1} for phosphate) [26]. Therefore, designing a NASICON cathode based on the appropriate stoichiometry of mixed polyanion with an iron (Fe) redox couple such as sodium iron phosphosulfate, $NaFe_2PO_4(SO_4)_2$ would be promising as high energy density cathodes for NIBs. One of the early works on $NaFe_2PO_4(SO_4)_2$, reported by Goodenough et al., exhibits a reversible capacity of 100 mAh g^{-1} at 0.1C at the 50th cycle [27]. The major drawback of $NaFe_2PO_4(SO_4)_2$ is an extensive polyanion network, which leads to poor electrical conductivity and a significant loss in capacity [20]. Polyanion networks provide high electronegativity which leads to increase in the band gap [25]. Higher band gap requires additional energy for electron transfer to the conduction band from the valence band, which leads to poor electrical conductivity. Lower electrical conductivity is detrimental to the overall electrochemical performance of the material.

To overcome these drawbacks, various strategies have emerged to enhance the performance of $NaFe_2PO_4(SO_4)_2$. One prevalent approach involves carbon coating, which is achieved by introducing conductive carbonaceous materials like graphene, carbon nanotubes, and carbon nanoparticles during the synthesis process [16,28]. Wu et al. [29] synthesised $NaFe_2PO_4(SO_4)_2$ by introducing reduced graphene oxide which showed a specific capacity of 90 mAh g^{-1} (at 25 mAg^{-1} current density) which is higher compared to the pristine sample. Introducing such carbons, strategy aims to improve electrical conductivity and facilitate better electron and ion transport within the material. Furthermore, two other strategies have shown promise: particle size reduction and cation doping [30,31]. Reducing particle size allows sodium ions to access remote regions within the electrode more effectively. Cation doping, on the other hand, involves introducing metal ions with larger ionic radii into the Fe sites of the material to expand its lattice parameters, thereby enhancing the electrochemical performance of NIBs. In addition to this, doping of cations can significantly improve ionic conductivity and structural stability while limiting undesirable phase transitions, metal-ion dissolution, and oxygen evolution [32].

In one of the works, Hamdi et al. [33] prepared pure $NaFe_2(PO_4)(SO_4)_2$ powder sample using a sol–gel reaction route, which delivered a specific discharge capacity ~78 mAh g^{-1} at C/10 and 96 % capacity retention (at C/5) after 30 cycles. It was observed that the cathode exhibits inferior performance due to poor sodium-ion diffusion, and low electrical conductivity. Rachid et al. [34] further improved the performance of $NaFe_2(PO_4)(SO_4)_2$ by doping Vanadium and introducing a carbon network (using citric acid as carbon source) to prepare $NaFe_{2-x}V_x(PO_4)(SO_4)_2$ (x = 0.2, 0.4, 0.6, 0.8, and 1.0). The optimized composition here, $NaFe_{1.6}V_{0.4}(PO_4)(SO_4)_2$, show superior electrochemical performance with a specific capacity of ~85 mAh g^{-1} at C/10. Despite such strategies to boost performance, $NaFe_2PO_4(SO_4)_2$ has received limited interest, perhaps due to the complications associated with the sol–gel route commonly used for its synthesis [27,33–37]. Sol-gel synthesis involves multiple steps with difficulty in controlling the reaction and poses limitations with scalability. Therefore, a chemo-mechanical route was adapted for synthesis for our present research.

Herein, we introduce a new method to enhance the performance of a $NaFe_2PO_4(SO_4)_2$ cathode by incorporating magnesium (Mg^{2+}) as a dopant. This was achieved through a straightforward solid-state reaction using a chemo-mechanical synthesis approach, with multi-walled carbon nanotubes (MWCNT) as a conductive additive. Mg was chosen as a dopant due to its cost-effectiveness, abundance in the earth's crust, and relatively low atomic mass. The as-prepared $NaFe_{2-x}Mg_xPO_4(SO_4)_2$ at x = 0.05 showed remarkable enrichment in sodium-ion uptake, especially regarding energy density, rate capability, and cycling stability. It delivered a reversible capacity of about 111 mAh g^{-1} and 86 mAh g^{-1} at current rates of C/20 and C/5, respectively, with 86.45 % capacity retention over 100 cycles (at C/5). Further, ex-situ XRD was carried out on doped and undoped samples of $NaFe_{2-x}Mg_xPO_4(SO_4)_2$, which shows a drastic reduction in structural distortions post doping due to enlarged lattice parameters which, consequently, reduces the lattice strain for reversible sodiation.

2. Experimental section

2.1. Synthesis $NaFe_{2-x}Mg_xPO_4(SO_4)_2$ samples

For the synthesis of $NaFe_{2-x}Mg_xPO_4(SO_4)_2$ (NFMPS) samples, NaH_2PO_4 (Sigma Aldrich, ≥ 99 %), $FeSO_4{\cdot}7H_2O$ (S.K. Traders, India, ≥ 98 %) and $MgSO_4{\cdot}7H_2O$ (Sigma Aldrich, ≥ 98 %) were used as starting precursors for material synthesis. $FeSO_4{\cdot}7H_2O$ and $MgSO_4{\cdot}7H_2O$ were dried at 300 °C for 20 hrs in an argon atmosphere to remove water. Then, the dried $FeSO_4$ and $MgSO_4$ were mixed with NaH_2PO_4 in stoichiometric proportions and ball-milled at 400 rpm for 12 hrs under an argon atmosphere. The resulting, white-coloured powder was further calcined for 7 hrs at 550 °C in an argon environment. Additionally, to improve the electrical conductivity of the samples, 10 wt% MWCNT (Adnano Technologies India, ≥ 99 %) was added as a conducting additive and ball-milled at 150 rpm for 12 hrs. Finally, the obtained product was reheated at 550 °C for 7 hrs under argon flow to yield the conducting additive mixed final product of NFMPS, which was stored in a glovebox (with < 0.1 ppm H_2O and O_2 content). The Mg dopant concentration in NFMPS was adjusted as 0,0.01,0.03,0.05,0.07, and 0.1 mol by changing $MgSO_4$ precursor content in the solid-state reaction and the obtained compounds were labeled as NFMPS00, NFMPS01, NFMPS03, NFMPS05, NFMPS07, and NFMPS10, respectively. In order to understand the effect of MWCNT, NFMPS00 and NFMPS05 were synthesised in a similar fashion by replacing MWCNT with carbon black (CB), labelled as NFMPS00-CB, and NFMPS05-CB.

2.2. Material characterisation

To investigate the crystal structure and phase purity of all NFMPS samples, powder X-ray diffraction (PXRD) was performed using a PANalytical Empyrean XRD diffractometer with Cu-Kα radiation (λ = 1.54 Å) at ambient conditions. The data were collected in 2θ range of 10° – 90° (scan rate of 0.013° s^{-1}). The Rietveld refinement was performed using the Fullprof program package to match the observed XRD patterns. The peak profiles were determined during this refinement using a well-

known pseudo-Voigt function. VESTA (Visualisation for Electronic Structural Analysis) was used to represent the crystal structure of prepared samples and their 3D representations. Thermogravimetric analysis (TGA) was employed to determine the decomposition temperature of all NFMPS samples. This investigation was carried out using a PERKIN ELMER TGA-8000 instrument in the temperature range of 50 °C to 800 °C at a ramp rate of 5 °C min^{-1}.

The particle morphology and chemical composition of the as-prepared samples were examined using a high-resolution field emission scanning electron microscope (HR-FESEM, Zeiss ULTRA Plus, GeminiÒ column with theoretical resolution of 1.0 nm at 15 kV) coupled with semi-quantitative energy-dispersive X-ray spectrometry (EDX). High-resolution transmission electron microscopy (HRTEM) coupled with selected area electron diffraction (SAED) was performed on a Hitachi HF5000 Cs-STEM/TEM at an acceleration voltage of 200 kV. Further, the quantitative information about the physical properties of synthesized particles, such as size, roughness, and surface texture, was obtained *via* Atomic Force Microscopy (AFM) using an Agilent Technologies AFM instrument. The specific surface area of prepared samples was investigated by Brunauer −Emmett-Teller (BET) using N_2 adsorption/desorption experiment (Nova 600 BET, Anton Paar). X-ray photoelectron spectroscopy (XPS) (Kratos AXIS Supra Plus, monochromatic Al Kα X-ray source) technique was employed to determine the chemical environment and electronic states of iron within NFMPS. The electrical conductivity measurements were performed using a linear two-point probe system. Further, to investigate the structural integrity of NFMPS00 and NFMPS05 during the interaction of Na^+, an ex-situ XRD analysis was performed as follows: both cathodes were charged and discharged at different cell voltages, and then coin-cells were disassembled in the glove-box. All electrodes were rinsed multiple times using propylene carbonate (PC) to remove the deposited salts and then dried in a vacuum oven at 40° C.

2.3. Electrode fabrication

The slurry of the working electrode was prepared by mixing 72 wt% of cathode material, 18 wt% conducting additive, and 10 wt% of polyvinylidene fluoride (PVDF) binder in N-Methyl-2-pyrrolidinone (NMP) solvent. The overall conducting additive, i.e., MWCNT, was maintained as 18 wt%, considering the prior addition during active material synthesis. Unless stated otherwise, MWCNT is the conducting additive used for electrode fabrication. A mortar and pestle was used to grind the sample to form a uniform slurry and then cast onto Al-foil via a manual doctor blade method. The average mass loading of active material was around 1.5–2.0 mg cm^{-2}. Then, the dried electrode was obtained by evaporating NMP in a vacuum oven at 100 °C overnight. Finally, the resulting electrode film was punched into a circular disk for assembly into a coin cell.

2.4. Electrochemical measurements

Electrochemical measurements of all NFMPS samples were performed using CR2032 coin cells. Pure sodium metal was used as both counter and reference electrode. The electrolyte used here was 1 M sodium perchlorate ($NaClO_4$, Sigma Aldrich, ≥ 98 %) solubilised in propylene carbonate (PC, Sigma Aldrich, ≥ 99 %) with 10 % (v/v) and fluoroethylene carbonate (FEC, Sigma Aldrich, ≥ 99 %) as electrolyte additives. The coin cell was assembled in a high-purity argon-filled glove box (with < 0.1 ppm H_2O and O_2 content) while using glass fibre (Whatman GF/C) as the separator. Room temperature galvanostatic charge/discharge cycling tests were performed using a Neware battery cycler in the voltage window of 2.0–4.4 V (*vs.* Na/Na^+) at different current rates (C-rates). The cyclic voltammetry (CV) tests were carried out in the same voltage domain of 2.0–4.4 V (*vs.* Na/Na^+) at various sweep rates of 0.1, 0.25, 0.50, 0.75, and 1 mV s^{-1} using Metrohm Autolab workstation. The electrochemical impedance spectroscopy (EIS) technique was also performed to determine the overall resistance offered during Na^+ transport from the bulk of solution to the surface of the electrode in the frequency range of 100 kHz to 0.05 Hz with an amplitude of 10 mV. Further, the Galvanostatic Intermittent Titration Technique (GITT) was used to determine the sodium-ion diffusion coefficient for all NFMPS samples.

2.5. Density functional theory (DFT) calculations

Kohn-Sham DFT simulations were performed on NFMPS00 and NFMPS05 structures by employing the Vienna Ab Initio Simulation Package (VASP) [38–40]. The initial structure of NFMPS05 was prepared by randomly replacing the appropriate fraction of Fe atoms in NFMPS00 ($NaFe_2PO_4(SO_4)_2$) with Mg. The crystal structure of NFMPS00 and NFMPS05 was optimized by allowing the ionic positions, size, and shape of the simulation box to change using the Perdew-Burke-Ernzerhof (PBE) function modified for solid materials [41] with the projector augmented wave (PAW) method [42]. A 4 × 4 × 2, Γ-centred k-point mesh and 520 eV energy cutoff for the plane-wave basis was employed for the optimization calculations. The electronic and ionic relaxation convergence criteria were set to 10^{-4} eV and 0.01 eV $Å^{-1}$, respectively. Total density of states (DOS) of the undoped and Mg doped NASICON structures were analysed using the VASPKIT code [43].

3. Results and discussion

3.1. Material

The synthesis of NFMPS is schematically represented in Fig. 1. MWCNT was introduced into the material as a conducting additive to facilitate the easy transport of electrons. Using a facile ball milling approach, all solid-state reactions of precursors enabled a one-pot synthesis protocol. As shown in Fig. 2a, TGA measurements showed a steep decrease in weight beyond 550 °C for all NFMPS due to decomposition of the samples. Therefore, 550 °C was used to fuse the precursors to form NFMPS during synthesis. Once the reaction was completed, XRD was performed for all samples at different dopant ratios (Fig. 2b), confirming the formation of a NASICON type structure [34]. No new diffraction peaks were observed in XRD analysis over the entire range of 2θ for the doped samples, indicating that Mg-ions have been successfully incorporated on the Fe-sites without altering the material's structure. The overall makeup of NASICON type NFMPS relies on organising octahedral components of Fe/MgO_6 with the tetrahedral components of P/SO_4 via sharing O atoms at the corners.

The crystallographic orientation was confirmed via XRD, which shows a NASICON-structured NFMPS for all compositions. The obtained structure displayed four types of interstitial sites (at 3a, 3b, 9d, and 9e) for the occupation of sodium atoms and vacancies (Tables S3 and S4). Further, to obtain accurate phase information for the undoped and doped samples, the XRD data was analysed via Fullprof software, and the results are shown in Fig. 2c and d, respectively. The Rietveld refinement was conducted using space group R-3 (ICSD No. 148). The calculated lattice parameters and the atomic positions of NFMPS00 and NFMPS05 are shown in Tables S1- S4, respectively. To gain an understanding of the interatomic distances and bond valances, the doped NFMPS05 sample was further analysed (Table S6). The average Fe-O distances for Fe1 is c.a. 1.983 Å, and that for Fe2 is c.a. 2.025 Å for the FeO_6 octahedra in the crystal structure of NFMPS05. Further, these average distances match the effective radius (r_{eff} = 1.950 Å) in a six-coordinated Fe^{3+} and O^{2-} [44]. The values of bond valance sum for Fe1 and Fe2 are 3.486 and 3.013, respectively, which show that Fe1 is more over-bonded than Fe2 [45,46], and the P1/S1O_4 tetrahedra were strongly distorted. Similarly, the d(P1/S1-O) distances range from ~1.420 Å to ~1.745 Å with a mean value of ~1.560 Å. The observed mean value is slightly higher than the r_{eff} of for four coordinated P^{5+}–O^{2-} (1.550 Å) and S^{6+}–O^{2-} (1.500 Å). Also, the $Na1^+$ and $Na2^+$

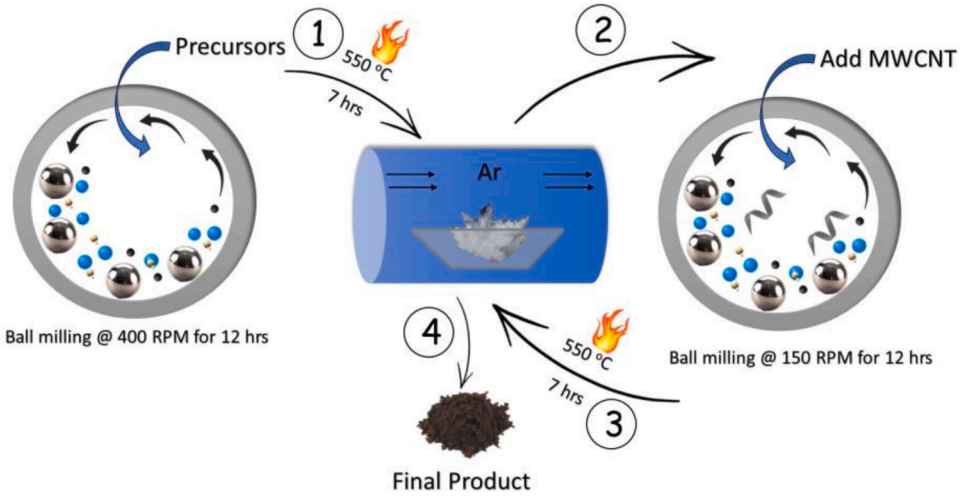

Fig. 1. Schematic representing the steps involved in the synthesis of all NFMPS samples.

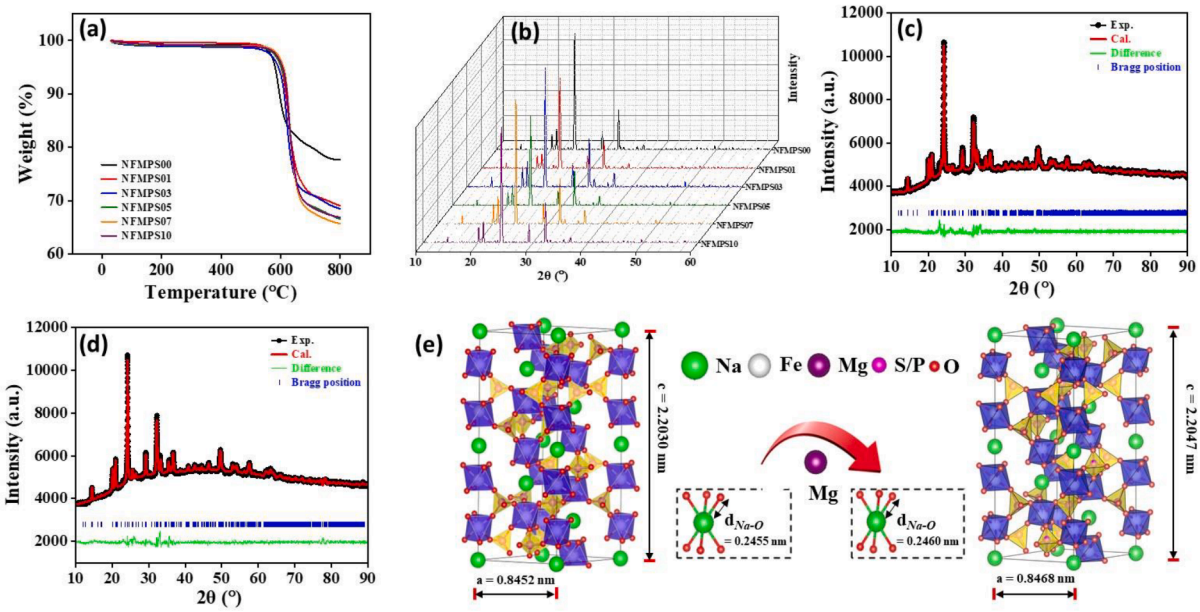

Fig. 2. (a)Thermogravimetric analysis and (b) XRD patterns of all NFMPS samples. Rietveld refined patterns of (c) NFMPS00 and (d) NFMPS05. (e) Schematic representing the effect of Mg-ion doping in NFMPS.

cations are surrounded by six (O^{2-}) anions. The average atomic distances estimated for Na1-O (~2.460 Å) and Na2-O (~2.501 Å) were larger than that of the r_{eff} of Na^{+} and O^{2-} (2.420 Å) [44]. The bond valance sums of 1.061 and 0.813 for Na1 and Na2, respectively, reveal that Na2 was slightly under-bonded. Further, compared with NFMPS00 data (a = b = 8.4520 Å, and c = 22.0300 Å), the cell parameters (a = b = 8.4680 Å, and c = 22.0470 Å) of NFMPS05 illustrates that Mg-ion doping enlarges the lattice parameters and creates the distortion in crystal framework (Fig. 2e). The unit cell volume of NFMPS05 (1369.1532 $Å^3$) was moderately higher than that of NFMPS00 (1362.9101 $Å^3$), signifying a little structural change in NFMPS00. This could be due to the ionic radius of Mg (r = 0.65 Å) being slightly higher than that of Fe (r = 0.64 Å). Moreover, the extended lattice parameters *via* Mg-ion doping could enhance Na^{+} diffusion and storage. The bond length of Fe-O, P/S-O, and Na-O increases considerably with Mg-ion doping (Table S5), indicating the possibility of enhanced diffusion pathways for sodium-ion, leading to better charge transport at high current rates [47,48].

To evaluate the valence state of Fe in all NFMPS samples, the X-ray photoelectron spectra (XPS) were obtained (Fig. S4). Among them, the two peaks observed in the deconvoluted Fe $2P_{3/2}$ spectra at ~711 and ~714 eV were the characteristic peaks of Fe^{2+} and Fe^{3+}, respectively [49,50]. Similarly, the two peaks deconvoluted at ~724 and ~427 eV belong to Fe^{2+} and Fe^{3+} (Fe $2P_{1/2}$), respectively. The oxidation of iron from Fe^{2+} to Fe^{3+} has been recognized as one of the common phenomena during the synthesis of materials [50–53]. Further, the satellite peak positioned at ~717 eV is associated with Fe $2P_{3/2}$, which aligns with the literature [54,55]. The microstructure of undoped NFMPS00 and doped NFMPS05 was analyzed by FESEM (Figs. S1 and S2). The FESEM images show the aggregate of as-prepared compounds with MWCNT interwoven within the structure. Also, adding Mg-ion dopant slightly varies the morphology by reducing particle size and changing the texture from bulky to flakier. Furthermore, the EDX mapping display a uniform distribution of Na, Fe, P, O, S, and Mg and their stoichiometric proportions in atom% for NFMPS00 and NFMPS05 were observed through the EDX spectra (Fig. S1c–k and S2c-l).

The HRTEM images (Fig. 3a and b) of NFMPS05 also reveal the even distribution of MWCNTs among the particles and provide better

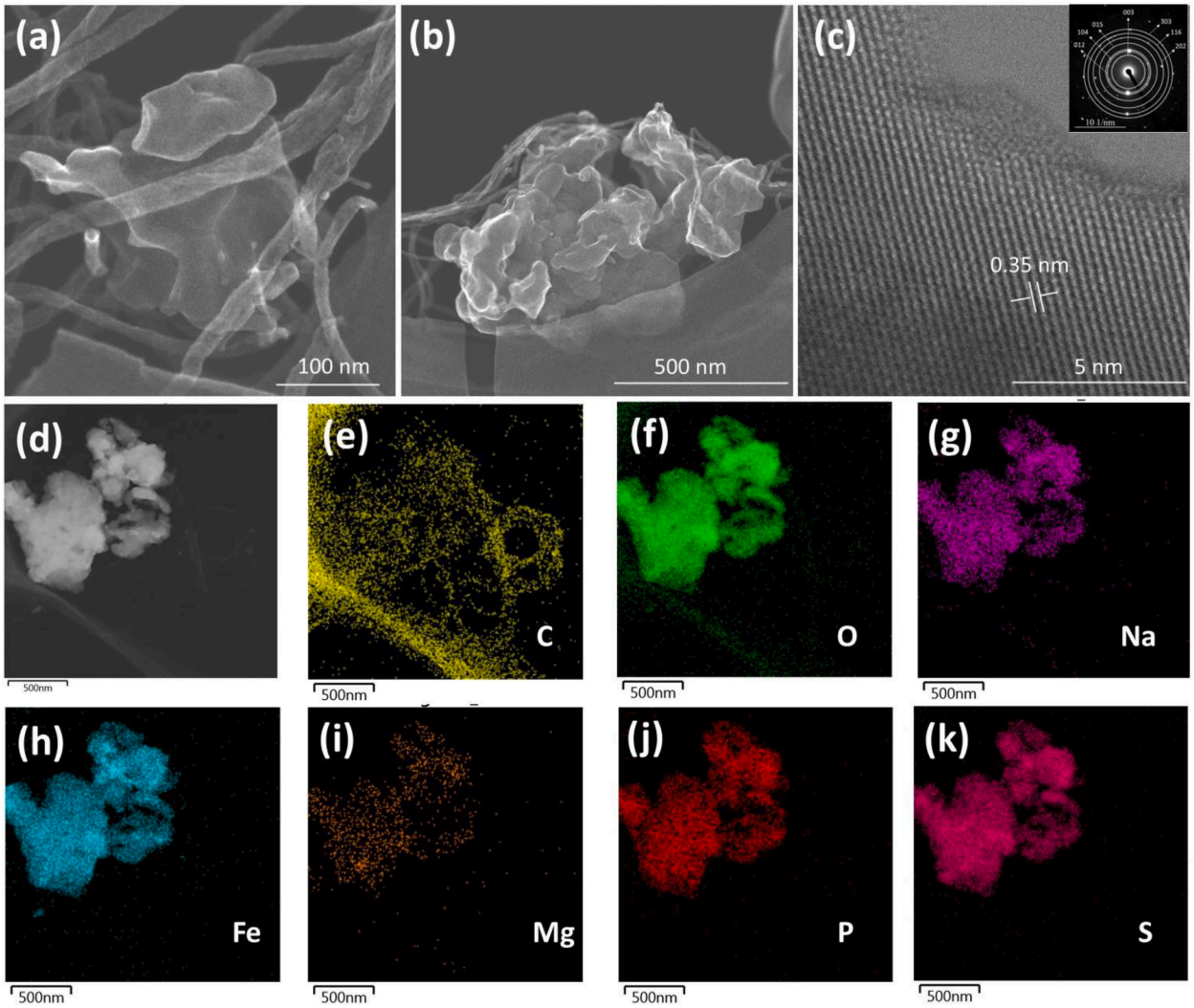

Fig. 3. (a, b) TEM images, (c) enlarged lattice fringes and SAED in the inset, (d) electron image and (e − k) EDS mapping of all elements in the sample of NFMPS05.

conductive channels for electron transfer and sodium ion diffusion. Fig. 3c displays the lattice fringes of the magnified image of NFMPS05. The observed lattice spacing of 0.35 nm could be indexed to the (1 1 3) planes of Trigonal NFMPS05.

Further, Fig. 3c inset exhibits the selected area electron diffraction (SAED) patterns of NFMPS05. The series of strident spots observed in SAED reveals the presence of a long-range ordered structure of cathodes. The electron image and EDX results are shown in the Fig. 3d-k. The elements such as C, O, Na, Fe, Mg, P, and S are uniformly distributed in the NFMPS05. Further, Fig. S3 displays the EDX spectra, which showcase all the elements present in NFMPS05 with near stoichiometric proportions.

3.2. Electrode optimisation

To investigate the electrochemical performance of all synthesised NFMPS cathodes in NIBs, the active material, binder, and conducting additive were ground using a mortar and pestle and pasted onto an Al-current collector to make the electrodes. It was initially observed that the coating made via grinding in the mortar had coarser particles that could eventually prevent electrolytes from percolating into the electrode post-battery fabrication. Therefore, the coating process was optimised by ball-milling the slurry mixture at 0, 5, 10, 15, and 20 h at 400 rpm. The electrode mixture ball-milled at the above timeframes was coated onto the Al-foil and tested against sodium metal as the counter electrode and $NaClO_4$ in PC with FEC additive as the electrolyte. NFMPS05 was chosen as the active material for this study. The cyclic voltammograms (CV) indicate an increase in peak current with an increase in ball milling time. 15 h of ball milling at a speed of 400 rpm shows the highest peak current, with no evident increase in peak current at 20 h of ball milling at the same speed (Fig. S5a). Further, the galvanostatic charge–discharge (GCD) curves indicate the highest specific capacity of around 96 mAh g^{-1} at a current rate of C/10 for 15 hrs of ball-milling and no further increase in specific capacity at 20 hrs of ball milling (Fig. S5b). Similar observations were also made for cycling stability studies with the optimum ball milling time for the electrode mixture for 15 hrs, and no observable changes in electrochemical performance were recorded (Fig. S5c).

AFM images for the cast electrode at different ball-milling times are shown in Fig. S6. The roughness profiles (Fig. S7) obtained for the samples show a sharp decrease in R_a (3.5 μm for no ball milling *vs*. 0.93 μm for 15 hrs ball milling) and R_q (4.3 μm for no ball milling *vs*. 1.2 μm for 15 hrs ball milling) with the progression of time. These values stabilise after 15 hrs of ball milling with no noticeable changes in these values. Hence, ball milling made the electrode mixture finer, enabling contact and allowing better electrolyte wetting. Further, Brunauer-Emmett-Teller (BET) N_2 sorption analysis was performed to investigate the surface area of NFMPS05 samples ball milled at 0 h and 15 h. Fig. S8a (0 h) and b (15 h) represents the adsorption/desorption isotherms. The specific surface area obtained for 15 hrs NFMPS05 sample was around 33.506 m^2/g, which was significantly more than 0 hrs of

NFMPS05 (29.758 m^2/g). The higher specific surface area is mainly responsible for complete electrolyte percolation and Na^+ transport within the electrode, which can significantly enhance the performance of the cathode material [56,57]. Therefore, based on these observations, all the electrode mixtures for different Mg-ion dopant concentrations were carried out at 15 hrs ball mill time and cast onto Al-foil via a manual doctor-blade method for further studies.

3.3. Electrochemical performance

To confirm the enhancement of sodium-ion uptake post-Mg-ion doping in NFMPS, they were tested as cathodes in a half-cell configuration with sodium metal as the counter electrode and $NaClO_4$ in PC with FEC additive as the electrolyte. All the electrochemical tests were carried out in the 2.0 to 4.4 V voltage range *vs.* Na/Na^+. Also, the casting onto Al-foil for all samples was made after 15 hrs of continuous ball milling of the electrode mixture. The GCD studies of all the samples were carried out at a current rate of C/20 (1C = 127 mA g^{-1}). The initial specific capacities for NFMPS00, NFMPS01, NFMPS03, NFMPS05, NFMPS07, and NFMPS10 were observed as 85, 90, 97, 111, 95, and 82 mAh g^{-1} respectively at current rate of C/20 (Fig. 4a). A discernible rise in specific capacity is evident as the Mg-ion doping content increases. This trend could stem from an augmented charge-transfer rate facilitated by the expansion in the lattice parameters of the structure. Remarkably, the optimal performance was achieved for NFMPS05. Beyond this point, a subsequent increase in Mg doping led to a reduction in specific capacity due to the decrease in the availability of Fe to partake in the redox reaction. For the sample NFMPS05, a reversible charging and discharging capacity of 125 and 111 mAh g^{-1} was observed.

In addition to this, Fig. 4a shows an elevated discharge voltage with minimum electrochemical polarisation for NFMPS05 as compared to NFMPS00. For an in-depth analysis of voltage polarization, a graph between current intensity ($I_{applied}$) *vs.* the charge/discharge voltage difference (ΔE) for NFMPS00, and NFMPS05 were plotted in Fig. S14a. The voltage difference (ΔE) values were extracted from the mid of charge/discharge plot. (i.e., at the half capacity point) at different C-rates for both the samples. The profile of $I_{applied}$ *vs.* ΔE is indicative of the type of polarization. A linear behaviour shows an Ohmic polarization, while an exponential behaviour shows a charge transfer polarization [58,59]. The obtained results in Fig. S14a, clearly demonstrate that the overall overpotential is mainly controlled by charge transfer polarization. It can be observed from Fig. S14a, that the NFMPS05 shows the minimum cell polarisation compared to NFMPS00 even at high current rates. Further, the cycling stability test (Fig. 4b) for all the samples was carried out at C/5 for 100 cycles. The samples NFMPS00, NFMPS01, NFMPS03, NFMPS05, NFMPS07, and NFMPS10 delivered an initial reversible specific capacity of 72, 74, 80, 86, 78, and 73 mAh g^{-1}, respectively (Fig. 4b). Even after 100 cycles, ~75 mAh g^{-1} capacity was retained by the sample of NFMPS05 with only ~13 % loss in capacity. As compared to the other samples, the cycling stability (Figs. S9 and S10) is significantly high for NFMPS05 even at higher current rates of 1C and 2C (Figs. S11 and S12). Similar observations were made while assessing the rate tolerance of samples (Fig. 4c), where they were subjected to various current rates from C/20, C/10, C/5, 1C, 2C, 5C, and C/10 for 4 cycles each, and the C rate was reinstated to C/20 for the final 4 cycles. Fig. S13 (d, e) and Table S7 shows the values obtained for various C-rates in the rate tolerance study. Among all the samples, the NFMPS05 showed better capacity retention (111 mAh g^{-1} at first cycle *vs.* 102 mAh g^{-1} at 36 cycle) when the C-rate was reinstated to C/20 after deep cycling at various rates. The above results show that the Mg-ion dopant significantly enhances the electrochemical performance. Also, stark differences in specific capacity can be seen with varying Mg dopants NFMPS.

Additionally, to understand the effect of Mg-doping alone on the NFMPS electrodes, NFMPS00-CB and NFMPS05-CB samples were synthesised by incorporating an equal amount of carbon black (18 wt%) by replacing the MWCNT. The samples were tested in similar operating conditions using similar electrolyte compositions used for samples that contain MWCNT. The electrochemical studies for these samples are shown in Fig. S14. NFMPS05-CB (Fig. S14b) delivers a discharge specific capacity of 94.36 mAh g^{-1} which is higher than the NFMPS00-CB (84.85 mAh g^{-1}) at a current rate of C/20. The comparative discharge specific capacities at a high current rate of 2C for NFMPS00, NFMPS05, NFMPS00-CB, and NFMPS05-CB are also presented in Fig. S14c. NFMPS05 provides a higher specific discharge capacity over the entire

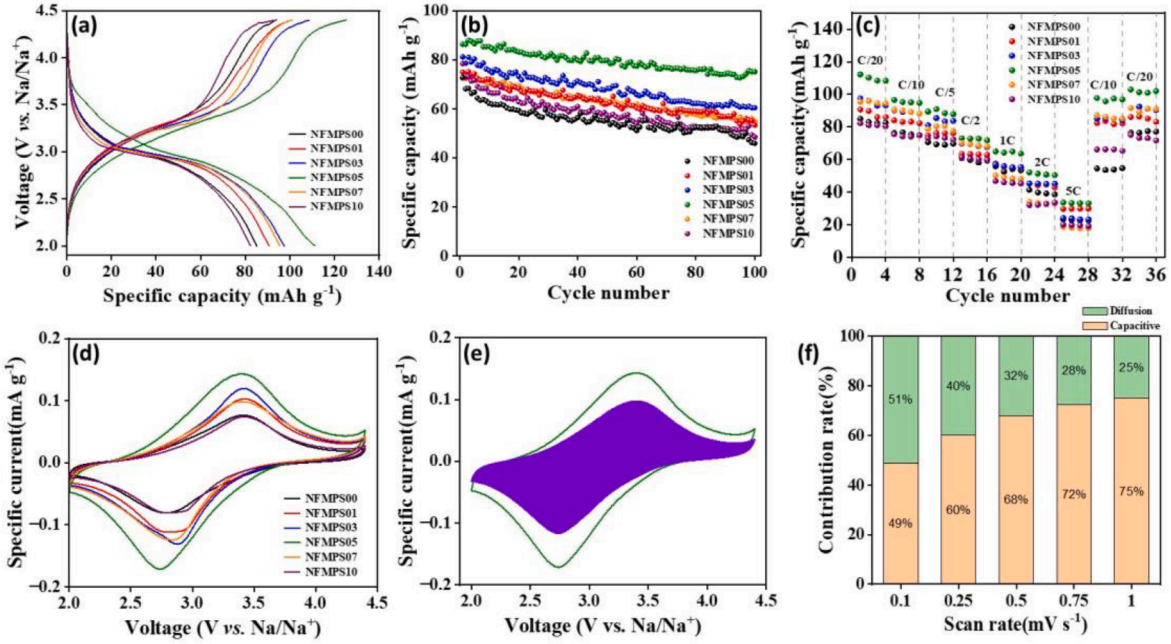

Fig. 4. (a) GCD curves (at C/20) and (c) rate tolerance studies for all the NFMPS samples. (b) cycling stability studies (at C/5), (d) all samples CV at 0.50 mV s^{-1}, (e) CV (at a scan rate of 0.50 mV s^{-1}) of NFMPS05 showing capacitive contribution, and (f) the percentage of capacitive contribution at different scan rates for the sample NFMPS05.

100 cycles compared to all others. From these observations, one can conclude that the addition of MWCNT with optimum Mg-doping boosts the electrochemical performance of the NFMPS05.

Fig. 4d shows the sample's CVs were carried out in a half-cell configuration in the 2.2 to 4.4 V voltage range *vs.* Na/Na^+. The cathodic peak, representing Na-ion extraction, ranges from ~2.7 to ~3.0 V, and the anodic peak ranges from ~3.3 to ~3.5 V (Table S8) for the samples. The anodic–cathodic peak separation for the samples ranges from ~0.4 to ~0.7 V, respectively. Subjected to 5 cycles at a sweep rate of 0.25 mV s^{-1}, the CVs showed overlapping patterns (Fig. S15), implying a reversible process of sodium-ion extraction. Notably, the obtained CV curves exhibit broad profiles indicative of a single-phase reaction [27]. These findings are consistent with observations from the differential capacity plots, which correspond well with the CV outcomes. Kinetic studies on the obtained CVs were performed to understand the sodium-ion storage mechanisms. The CVs were recorded at various sweep rates of 0.1, 0.25, 0.5, 0.75, and 1 mV s^{-1} (Fig. S16).

Based on the data obtained from the CV of NFMPS samples (Fig. S16), peak current (i_p) was plotted against the square root of the scan rate ($v^{1/2}$). The total current contribution stemming from diffusion and capacitive controlled processes can be represented by using the following relation [60]:

$$i = k_1 v + k_2 v^{1/2} \quad (1)$$

Plotting ($i/v^{1/2}$) against ($v^{1/2}$) the values of k_1 and k_2 are determined as the slope and intercept, respectively. The capacitive and diffusion currents are determined by calculating k_1 and k_2 for the whole voltage range (2.0 – 4.4 V) for both positive and negative scans for a particular scan rate. A series of such current contributions for various scan rates of all the samples were calculated and represented in (Fig. S17). Fig. S18 shows the diffusion and capacitive contribution at various scan rates for all the samples. An intriguing trend emerges the capacitive contribution escalates with higher scan rates, unveiling a pseudocapacitive charge-storage behaviour that bolsters the overall capacity. Notably, as illustrated in Fig. 4e and f for NFMPS05, the capacitive contribution slightly surpasses that of the other samples, suggesting that optimising structures to enhance pseudocapacitive behaviours holds promise for improving sodium-ion uptake.

The confirmation of NFMPS samples pseudocapacitive behaviour is reinforced by the differential capacity (dQ/dV) plots. In contrast to the constant potential sweep rate used in a CV measurement, dQ/dV data is gathered at a constant current. These two sets of data complement each other in providing insights into the material's electrochemical behaviour. The dQ/dV profiles for the initial 5 cycles are illustrated in (Fig. S19). Notably, for NFMPS05, the curves of consecutive cycles exhibit a high degree of overlap, signifying reversible charge storage. In contrast, the other samples show a slight disparity between subsequent cycles. The coefficient of diffusion can be calculated from CV measurements using the Randles Sevick equation [61] as follows:

$$i_P = \left(2.69 \times 10^5\right) n^{3/2} A \left(D_{Na^+}^{1/2}\right) \left(C_{Na^+}\right) \left(\upsilon^{\frac{1}{2}}\right) \quad (2)$$

Here i_p is the peak current, n is the number of electrons transferred, A is the active surface area of the electrode, D_{Na+} is the diffusion coefficient of sodium-ion, C_{Na+} is the concentration of sodium-ion in the NFMPS, and υ is the scan rate. Fig. 5a shows a linear relationship between i_p and $\upsilon^{1/2}$, and the obtained slope from this curve is shown in Table S9. The sample's diffusion coefficients were shown in Fig. 5b and Table S10. Compared with the undoped sample, the Mg-ion doped samples show enhanced sodium-ion diffusion peaking for NFMPS05. The diffusion coefficient for extraction and insertion of Na^+ is 3.11 x 10^{-12} cm^2 $s^{-1}$and 2.80 x 10^{-12} cm^2 s^{-1} respectively.

Furthermore, the electrochemical characteristics and charge storage kinetics of NFMPS are also dependent on the electrical properties of material. In this context, conductivity measurements were carried out on all samples using a linear two-probe measurement system to investigate the impact of doping. Initially, around 1 g of each NFMPS powder was poured into the feeder of the tablet maker without any binder and

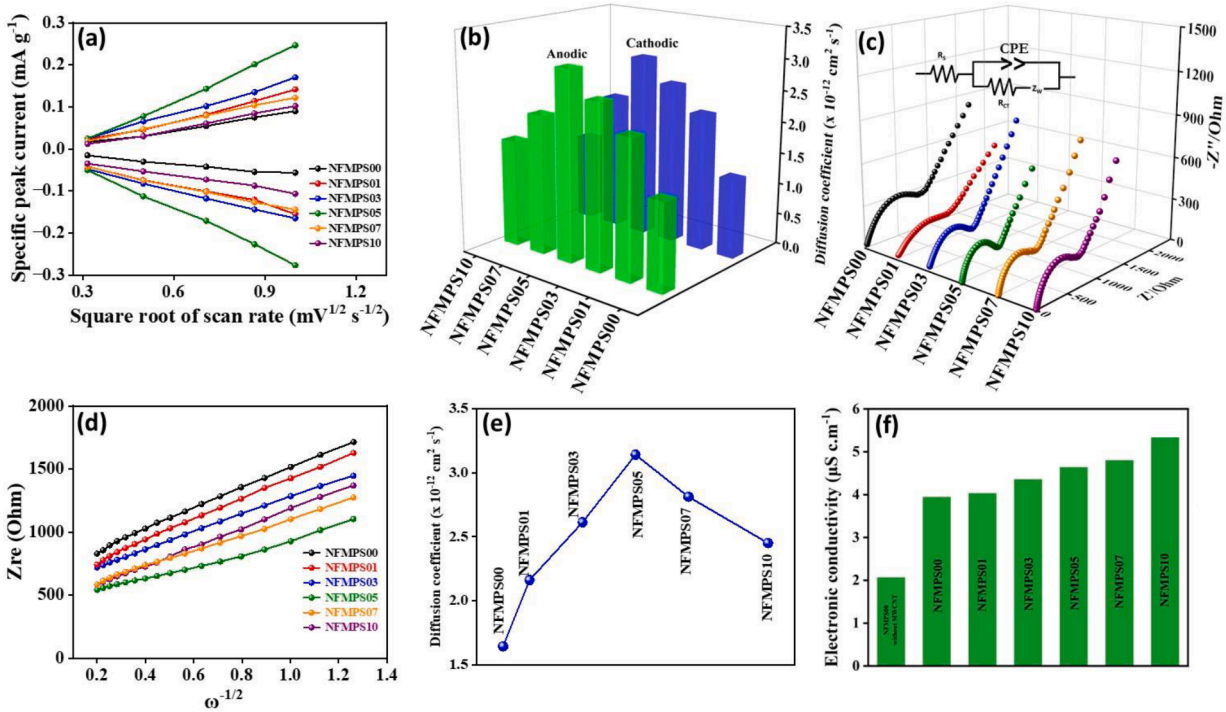

Fig. 5. (a) Peak specific current (i_p) *vs.* the square root of scan rate ($v^{1/2}$) at different scanning rates showing a linear relationship, (b) sodium-ion diffusion coefficients calculated based on a kinetic study of CV, (c) Nyquist plot; inset: the equivalent circuit used to analyze EIS, (d) the linear relation between Warburg impedance (Z_{re}) and inverse square root of angular frequency ($\omega^{-1/2}$), (e) sodium ion diffusion coefficient calculated from the plot (d), and (f) the comparison between electrical conductivity measured using two-point probe method of all NFMPS samples.

then pressed at the pressure of 100 MPa to make the pellets with a 10 mm diameter and average thickness of 0.52 mm. The measured electronic conductivity of all samples is displayed in Fig. 5f, revealing an increase in conductivity as the dopant concentration is raised. This phenomenon is attributed to the incorporation of Mg into Fe-sites to balance charges, where the holes generated by Fe-ions get compensated, subsequently leading to enhancement in conductivity [48]. The results shows that, the enhanced electronic properties of NFMPS after incorporating of Mg-ion are responsible for the boosted electrochemical performance of cathode material. Electrochemical impedance spectroscopy (EIS) was employed to delve deeper into the kinetics of the electrodes. Fig. 5c showcases Nyquist plots for all NFMPS samples. In these plots, a depressed semicircle is evident at higher frequencies, indicating the charge transfer resistance. Additionally, a straight line in the lower frequency range indicates the diffusion of Na^+ within the bulk of electrode [62–64]. The inset within Fig. 5c depicts the equivalent circuit used to fit the acquired EIS spectra (Fig. S20).

Within this circuit, R_s is the overall cell resistance, R_{ct} indicates the charge-transfer resistance, and Z_w represents the Warburg impedance, particularly determining charge-transfer diffusion limitations [65,66]. Detailed parameter values resulting from fitting are provided in Table S11. It was observed that the R_{ct} values decrease with increasing the dopant concentration from x = 0.0 to x = 0.05. This indicates that Mg-ion doping enhances ionic conductivity. Notably, among all the samples, NFMPS05 features the smallest R_{ct} value, signifying that Mg doping enhances the transport of sodium ions across the material. To understand the extent of charge transfer, diffusion coefficients were calculated for all the NFMPS samples. The coefficient of diffusion (D_{Na+}) can be deduced from plots within the lower-frequency region utilising the following equation:

$$D_{Na+} = \frac{R^2T^2}{2A^2n^4F^4C^2\sigma^2} \quad (3)$$

$$Z_{re} = R_s + R_{ct} + \sigma\omega^{-1/2} \quad (4)$$

Here, in the equation 3, R is the gas constant, T (298 K) is the temperature in Kelvin, A (1.1314 cm^{-2}) denotes the surface area, n is the number of electrons per molecule during oxidation, F (96,500 C mol^{-1}) is Faraday's constant, and C (4.98 x 10^{-3} mol cm^{-3} for NFMPS05) is the concentration of sodium ions calculated based on density and molecular weight [67].

The Warburg factor, denoted as σ, is related to Z_{re} (defined in equation 4); . As illustrated in Fig. 5d, the X-axis displays the inverse square root of frequency ($\omega^{-1/2}$), while the Y-axis portrays Z_{re} with the curves exhibiting linear behavior. The calculated diffusion coefficients from eqs. (3) and (4) are presented in Fig. 5e. Notably, the diffusion coefficient for NFMPS05 is 3.21 x 10^{-12} cm^2 $s^{-1,}$ which is higher than 1.64 x 10^{-12} cm^2 s^{-1} for the NFMPS00 undoped sample. This substantial increase underscores the significant enhancement in sodium-ion diffusion achieved by incorporating dopants. Further, the knowledge of the sodium diffusion coefficient (D_{Na+}) is essential for optimizing and designing cathode materials for NIBs. In this regard, the galvanostatic intermittent titration technique (GITT) was carried out to determine the D_{Na+} for all NFMPS electrodes as function working voltage in the range of 2–4.4 V. Fig. 6a represents the GITT curves that were recorded for all the samples at a current rate of C/10. Before performing the GITT, the cells were cycled for 10 cycles to reach a thermal equilibrium state. A simplified form of Fick's second law of diffusion was used to obtain the value of sodium-ion diffusion [68,69]:

$$D = \frac{4}{\Pi\tau}\left(\frac{m_B V_m}{M_B\, s}\right)^2\left(\frac{\Delta E_s}{\Delta E_\tau}\right)^2 \left(\tau \ll L^2/D\right) \quad (5)$$

where, m_B, V_m, M_B are the weight, molar volume, and the molar mass of the NFMPS cathodes respectively. ΔE_s, ΔE_τ, and s represents the quasi-equilibrium potential (achieved after 90 min of relaxation time), voltage change during applied current pulses (τ = 30 min), and the overall contact area of the electrode and electrolyte respectively. Fig. 6b illustrates the charging diffusion coefficient, and Fig. 6c shows the discharging diffusion coefficient for all NFMPS samples. The undoped NFMPS00 and doped NFMPS05 cathode materials reveals the D_{Na+} values of 3.27 x 10^{-11} cm^2 s^{-1}, and 5.25 x 10^{-11} cm^2 s^{-1} at 2.5 V (for charging) and 1.15 x 10^{-11} cm^2 s^{-1}, and 4.29 x 10^{-11} cm^2 s^{-1} at 2.6 V (for discharging) respectively. Similarly, D_{Na+} values of 3.2 x 10^{-12} cm^2 s^{-1}, and 6.9 x 10^{-12} cm^2 s^{-1} (for charging) and 2.50 x 10^{-12} cm^2 s^{-1},

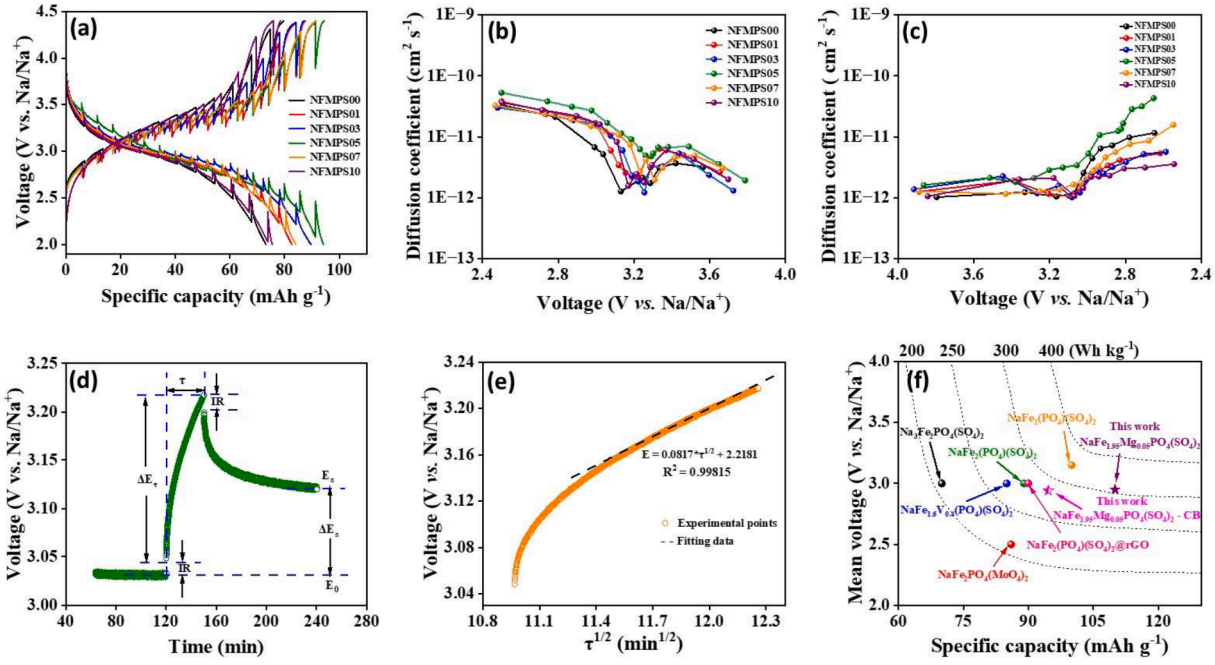

Fig. 6. (a) GITT curves at C/10 for 30 min of working time and 90 min of relaxation time for all NFMPS samples. From GITT, measured diffusion coefficients as a function of different (b) charging and (c) discharging voltages. (d) zoomed in Voltage profile for a single step of GITT curve at 3.2 V during the charge of NFMPS05 at C/10 and (e) corresponding linear behaviour of $\tau^{1/2}$ *vs.* V. (f) comparison of the energy density of NFMPS05 in the present work with that of other groups.

and 3.41 x 10^{-12} cm^2 s^{-1} (for discharging) obtained at 3.5 V for both NFMPS00 and NFMPS05 respectively, which shows agreement with the D_{Na+} results from CV analysis. It is also observed that the lower value of sodium ion diffusion at higher voltage for charging and discharging indicates high migration activation energy for the (de)intercalation of sodium ions in the vicinity of NFMPS [50]. Also, at ~2.5 V, the value of sodium-ion diffusion is maximum because of the steep increase in the voltage during charging [70] (Fig. 4a). For GITT, the electrodes were initially charged at a constant current rate of C/10 for 1800 s, followed by a relaxation period of 5400 s to reach a steady-state potential. This process continued until the cut-off voltage (i.e., V_{max} = 4.4 V and V_{min} = 2.0 V) was achieved. To illustrate this procedure, a single GITT profile for the charging process at voltage ~3 V is shown in Fig. 6d. Further, Fig. 6e shows a linear voltage behaviour with a square root of τ. Overall, the synthesized NFMPS05 showed an excellent sodium ion-storage capacity with a high cell voltage exhibiting an impressive energy density of 324 Wh kg^{-1} (Fig. 6f). The achieved energy density in our study is so far the highest amongst iron phosphosulfate cathodes reported in the literature (Table S12) [27,33–37].

Further, in order to understand the changes in the crystal structure of host cathode due to the reversible interaction of Na^+ during charge/discharge process, ex-situ XRD studies were performed for NFMPS00 and NFMPS05 samples at different charging and discharge voltages. The characteristic XRD peaks of both samples during the charging process i.e., from beginning to fully desodiated steps (patterns(a) to (e)), and discharging process i.e., from empty to fully sodiated steps (patterns (f) to (i)) for NFMPS00 and NFMPS05 are shown in Fig. 7a and b, respectively. It was observed that for NFMPS00 the peak positions corresponding to the planes (1 2–4), (303), and (131) slightly shifted towards the right during the charging process in comparison with the pristine electrodes before the electrochemical cycling. The charging process was followed by sodiation of NFMPS00 which also revealed a similar shift (Fig. 7a). This indicate that NFMPS00 show structural distortion over (de)sodiation. In contrast, the NFMPS05 samples maintained its structural integrity against Na^+ insertion and de-insertion as negligible shift in XRD peaks were observed. This can be attributed to the doping of Mg into NFMPS, which in turn enhances the lattice parameters facilitating the easy transport of Na^+ within the material. These results observed from the ex-situ XRD confirms that reversible uptake of Na^+ due to enlarged lattice parameters that regulate better charge diffusion in NFMPS05.

Moreover, the impact of Mg-ion doping on NFMPS crystal structure was examined in detail using first principles calculations. Here, a large supercell structure of NFMPS05 was prepared by incorporating Mg atoms in place of Fe in NFMPS00 crystals. The optimized trigonal crystal structure of NFMPS00, and NFMPS05 were shown in Fig. 7e and f respectively. The computed lattice parameters of a = 0.85 nm and c = 2.29 nm for NFMPS00 are well in agreement with our experimental values of a = 0.845 nm and c = 2.20 nm. This confirms that our DFT calculations were able to reproduce the experimental structural parameters of NFMPS. Further, it was observed that doping of Mg in NFMPS generates local structural distortion due to the extended Na-O bond length resulting in an increase in lattice parameters (as well as volume). This increase in bond length and volume has an important role in facilitating the movement of the Na^+ within the lattice framework. The DFT simulations therefore confirm our experimental observations that enhanced Na^+ transport was facilitated by Mg-ion doping. In addition to this, the effect of Mg substitution on the electrical conductivity of NFMPS was further analysed by computing the energy gap between the top of the valance band and the bottom of the conduction band. Fig. 7g and h, shows the total density of states (TDOS) for NFMPS00 and NFMPS05 respectively. The presence of Mg ions creates additional energy levels or alters the positions of existing energy levels, leading to changes in the DOS. It is worth noting that, the energy band gap of NFMPS05 was significantly reduced to 0.95 eV, which was much lower than that of NFMPS00 (1.52 eV). This reduced band gap energy demonstrates that the doping of Mg-ion in NFMPS enhances the electron transport, Na^+ kinetics, and reduces the energy migration barriers, thereby enhancing the overall sodium-ion uptake capabilities in NFMPS.

4. Conclusion

A novel all-solid-state synthesis of NFMPS with enhanced sodium-ion storage has been presented in our work, thanks to the Mg dopant and electronic conductivity offered by MWCNT. Material characterisation confirmed the NASICON structure, and XPS studies revealed the

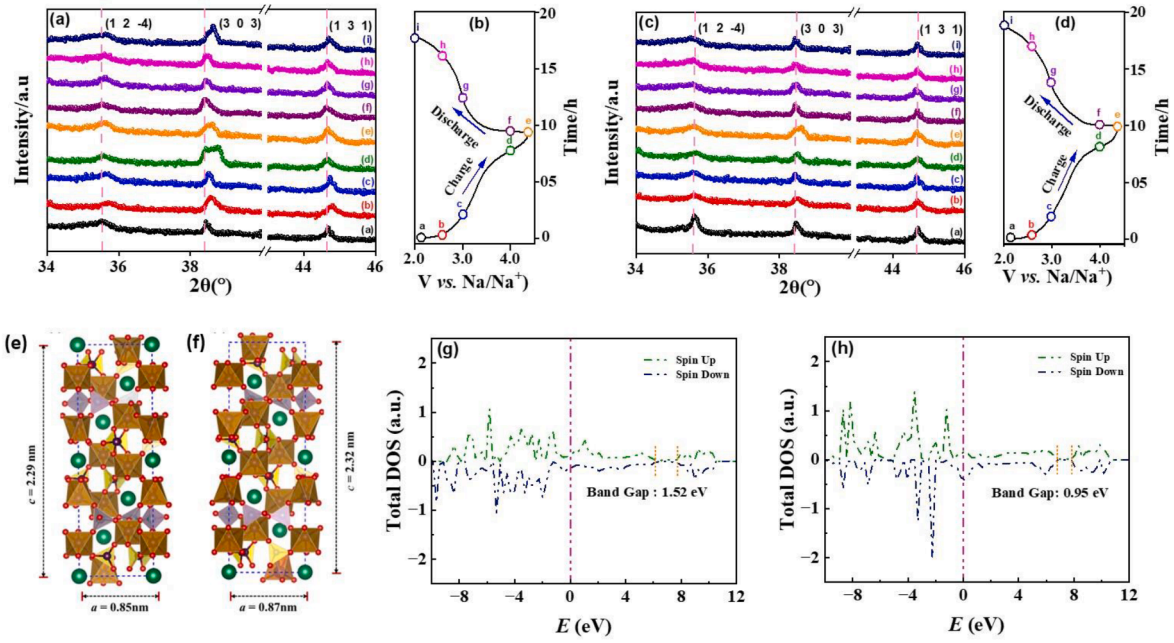

Fig. 7. Ex-situ characteristic XRD peaks of (a) NFMPS00, (c) NFMPS05, and corresponding charge-discharge profiles (b, d) [patterns (a: 2.05 V, b: 2.5 V, c: 3.0 V, d: 4.0 V, e: 4.4 V): charging (de-sodiation) process, and patterns (f: 4.0 V, g: 3.0 V, h: 2.5 V, i: 2.0 V): discharging (sodiation) process]. Optimised trigonal structure of (e) NFMPS00, (f) NFMPS05, and total density of states plots for (g) NFMPS00, (h) NFMPS05 crystal structures.

chemical environment of NFMPS. A working voltage as high as ~3 V *vs.* Na/Na^+ was obtained. The electrode fabrication was optimised with further ball milling for 15 h, and NFMPS05 showed a superior capacity, cycling stability, and an energy density of 324 Wh kg^{-1}. All samples of NFMPS were subjected to electrochemical tests and NFMPS05 displayed a capacity of 111 mAh g^{-1} at C/20 current rate, one of the highest obtained so far. The excellent sodium-ion storage in NFMPS stems from lower resistance for sodium-ion transport, as seen from the diffusion coefficient of ~10^{-11} to 10^{-12} cm^2 s^{-1}. Our research significantly contributes to the ongoing pursuit of developing efficient and cost-effective materials for advanced energy storage systems. Further, our study investigated using ex-situ XRD that the lower transport resistance was a consequence of enhanced lattice parameters which helps in maintaining the material stability during Na^+ (de)insertion within the electrode. Also, doping Mg increases the electrical conductivity of the electrode due to the reduction in the energy band gap which is also confirmed from the DFT calculations. Our work shows that mixed polyanion based, Mg-doped NFMPS engineered via a solid-state synthesis approach can enhance electrical/ionic conductivity, provide larger lattice parameters for better sodium-ion storage, and show excellent electrochemical performance against sodium, making it a promising cathode for advanced sodium-ion batteries.

CRediT authorship contribution statement

Sharad Dnyanu Pinjari: Writing – review & editing, Writing – original draft, Visualization, Validation, Investigation, Data curation, Conceptualization. **Ravi C. Dutta:** Writing – review & editing, Writing – original draft, Visualization, Software, Methodology, Formal analysis. **Shuimei Chen:** Writing – review & editing, Methodology, Investigation. **Purandas Mudavath:** Writing – review & editing, Visualization, Methodology. **Xiaodan Huang:** Writing – review & editing, Visualization, Validation, Software, Methodology. **John Bell:** Writing – review & editing, Writing – original draft, Visualization. **Suresh K. Bhatia:** Writing – review & editing, Writing – original draft, Visualization, Validation, Software, Resources. **Ashok Kumar Nanjundan:** Writing – review & editing, Writing – original draft, Visualization, Validation, Investigation. **Rohit Ranganathan Gaddam:** Writing – review & editing, Writing – original draft, Visualization, Validation, Supervision, Resources, Methodology, Investigation, Funding acquisition, Formal analysis, Data curation, Conceptualization.

Declaration of competing interest

The authors declare that they have no known competing financial interests or personal relationships that could have appeared to influence the work reported in this paper.

Data availability

Data will be made available on request.

Acknowledgements

Sharad Pinjari acknowledges IISER-Bhopal for providing fellowship for his PhD. Rohit Ranganathan Gaddam acknowledges the Department of Science and Technology (DST-SERB), Government of India for the Startup-Research Grant (SRG), SRG/2022/001017 for funding the work. The Central Instrumentation Facility of IISER-Bhopal is acknowledged for providing access to material characterisation facilities. This work used the Queensland node of the NCRIS-enabled Australian National Fabrication Facility (ANFF). AKN and JB acknowledge financial support from the Australian Research Council under the ARC Research Hub for Safe and Reliable Energy (IH200100035). This research was undertaken with the assistance of the computational resources provided at the NCI National Facility systems at the Australian National University (ANU), and those at the Pawsey Supercomputing Centre in Western Australia, through their National Computational Merit Allocation Schemes supported by the Australian Government and the Government of Western Australia.

Appendix A. Supplementary data

Supplementary data to this article can be found online at https://doi.org/10.1016/j.cej.2024.152485.

References

[1] Z. Yang, et al., Electrochemical energy storage for green grid, Chem. Rev. 111 (5) (2011) 3577–3613.
[2] V. Palomares, P. Serras, I. Villaluenga, K.B. Hueso, J. Carretero-González, T. Rojo, Na-ion batteries, recent advances and present challenges to become low cost energy storage systems, Energ. Environ. Sci. 5 (3) (2012) 5884–5901.
[3] J.B. Goodenough, Electrochemical energy storage in a sustainable modern society, Energ. Environ. Sci. 7 (1) (2014) 14–18.
[4] C. Delmas, Sodium and sodium-ion batteries: 50 years of research, Adv. Energy Mater. 8 (17) (2018) 1703137.
[5] J.-Y. Hwang, S.-T. Myung, and Y.-K. Sun, "Sodium-ion batteries: present and future," *Chem. Soc. Rev.,* 10.1039/C6CS00776G vol. 46, no. 12, pp. 3529-3614, 2017, doi: 10.1039/C6CS00776G.
[6] Y. Tian, et al., Promises and challenges of next-generation "beyond Li-ion" batteries for electric vehicles and grid decarbonization, Chem. Rev. 121 (3) (2020) 1623–1669.
[7] M. Li, J. Lu, Z. Chen, K. Amine, 30 years of lithium-ion batteries, Adv. Mater. 30 (33) (2018) 1800561.
[8] J. Xie, Y.-C. Lu, A retrospective on lithium-ion batteries, Nat. Commun. 11 (1) (2020) 2499.
[9] A. Manthiram, An outlook on lithium ion battery technology, ACS Cent. Sci. 3 (10) (2017) 1063–1069.
[10] C.P. Grey, D.S. Hall, Prospects for lithium-ion batteries and beyond—a 2030 vision, Nat. Commun. 11 (1) (2020) 6279.
[11] R.R. Gaddam, X.G. Zhao, Challenges and opportunities in sodium-ion batteries: an introduction, Handbook of Sodium-Ion Batteries (2023) 1–32.
[12] Y.-S. Hu and Y. Lu, "2019 Nobel prize for the Li-ion batteries and new opportunities and challenges in Na-ion batteries," vol. 4, ed: ACS Publications, 2019, pp. 2689-2690.
[13] A. Van der Ven, Z. Deng, S. Banerjee, S.P. Ong, Rechargeable alkali-ion battery materials: theory and computation, Chem. Rev. 120 (14) (2020) 6977–7019.
[14] K. Chayambuka, G. Mulder, D.L. Danilov, P.H. Notten, Sodium-ion battery materials and electrochemical properties reviewed, Adv. Energy Mater. 8 (16) (2018) 1800079.
[15] N. Yabuuchi, K. Kubota, M. Dahbi, S. Komaba, Research development on sodium-ion batteries, Chem. Rev. 114 (23) (2014) 11636–11682.
[16] S. Chen, et al., Challenges and perspectives for NASICON-type electrode materials for advanced sodium-ion batteries, Adv. Mater. 29 (48) (2017) 1700431.
[17] R.R. Gaddam, D. Yang, R. Narayan, K. Raju, N.A. Kumar, X. Zhao, Biomass derived carbon nanoparticle as anodes for high performance sodium and lithium ion batteries, Nano Energy 26 (2016) 346–352.
[18] B. Singh, et al., A chemical map of NaSICON electrode materials for sodium-ion batteries, J. Mater. Chem. A 9 (1) (2021) 281–292.
[19] M.T. Ahsan, Z. Ali, M. Usman, Y. Hou, Unfolding the structural features of NASICON materials for sodium-ion full cells, Carbon Energy 4 (5) (2022) 776–819.
[20] R. Rajagopalan, Z. Zhang, Y. Tang, C. Jia, X. Ji, H. Wang, Understanding crystal structures, ion diffusion mechanisms and sodium storage behaviors of NASICON materials, Energy Storage Mater. 34 (2021) 171–193.
[21] Q. Zhou, et al., Sodium superionic conductors (NASICONs) as cathode materials for sodium-ion batteries, Electrochem. Energy Rev. (2021) 1–31.
[22] Y. Wu, et al., Vanadium-free NASICON-type electrode materials for sodium-ion batteries, J. Mater. Chem. A (2022).
[23] C. Masquelier, L. Croguennec, Polyanionic (phosphates, silicates, sulfates) frameworks as electrode materials for rechargeable Li (or Na) batteries, Chem. Rev. 113 (8) (2013) 6552–6591.
[24] Y. You, A. Manthiram, Progress in high-voltage cathode materials for rechargeable sodium-ion batteries, Adv. Energy Mater. 8 (2) (2018) 1701785.
[25] P. Barpanda, Pursuit of sustainable iron-based sodium battery cathodes: two case studies, Chem. Mater. 28 (4) (2016) 1006–1011.
[26] D. Deb, G. Sai Gautam, Critical overview of polyanionic frameworks as positive electrodes for Na-ion batteries, J. Mater. Res. 37 (19) (2022) 3169–3196.
[27] K. Shiva, P. Singh, W. Zhou, J.B. Goodenough, NaFe 2 PO 4 (SO 4) 2: a potential cathode for a Na-ion battery, Energ. Environ. Sci. 9 (10) (2016) 3103–3106.
[28] W. Duan, et al., Na 3 V 2 (PO 4) 3@ C core–shell nanocomposites for rechargeable sodium-ion batteries, J. Mater. Chem. A 2 (23) (2014) 8668–8675.
[29] S.-F. Li, et al., Sponge-like NaFe 2 PO 4 (SO 4) 2@ rGO as a high-performance cathode material for sodium-ion batteries, New J. Chem. 45 (10) (2021) 4854–4859.
[30] L. Xiao, F. Ji, J. Zhang, X. Chen, Y. Fang, Doping regulation in polyanionic compounds for advanced sodium-ion batteries, Small 19 (1) (2023) 2205732.

[31] C. Zhu, K. Song, P.A. Van Aken, J. Maier, Y. Yu, Carbon-coated Na3V2 (PO4) 3 embedded in porous carbon matrix: an ultrafast Na-storage cathode with the potential of outperforming Li cathodes, Nano Lett. 14 (4) (2014) 2175–2180.
[32] B. Jeevanantham, P. Sarathkumar, S. Kavita, M. Shobana, Magnesium doped LiNixMnyCozO2 cathode-structural properties, Appl. Sur. Sci. Adv. 12 (2022) 100350.
[33] H.B. Yahia, R. Essehli, R. Amin, K. Boulahya, T. Okumura, I. Belharouak, Sodium intercalation in the phosphosulfate cathode NaFe2 (PO4)(SO4) 2, J. Power Sources 382 (2018) 144–151.
[34] R. Essehli, et al., Optimization of the compositions of polyanionic sodium-ion battery cathode NaFe2− xVx (PO4)(SO4) 2, J. Power Sources 469 (2020) 228417.
[35] Y. Wu, Z. Cao, L. Song, J. Gao, NaFe2PO4 (MoO4) 2: a promising NASICON-type electrode material for sodium-ion batteries, ACS Appl. Mater. Interfaces 13 (41) (2021) 48865–48871.
[36] S. Kumar, R. Ranjeeth, N.K. Mishra, R. Prakash, P. Singh, NASICON-structured Na 3 Fe 2 PO 4 (SO 4) 2: a potential cathode material for rechargeable sodium-ion batteries, Dalton Trans. 51 (15) (2022) 5834–5840.
[37] S.-F. Li, et al., Enhanced electrode kinetics and electrochemical properties of low-cost NaFe2PO4 (SO4) 2 via Ca2+ doping as cathode material for sodium-ion batteries, J. Mater. Sci. Technol. 78 (2021) 176–182.
[38] G. Kresse, J. Furthmüller, Efficiency of ab-initio total energy calculations for metals and semiconductors using a plane-wave basis set, Comput. Mat. Sci. 6 (1) (1996) 15–50, https://doi.org/10.1016/0927-0256(96)00008-0.
[39] G. Kresse and J. Furthmüller, "Efficient iterative schemes for ab initio total-energy calculations using a plane-wave basis set," *Phys. Rev. B,* vol. 54, no. 16, pp. 11169-11186, 10/15/ 1996, doi: 10.1103/PhysRevB.54.11169.
[40] G. Kresse and J. Hafner, "Ab initio molecular dynamics for liquid metals," *Phys. Rev. B,* vol. 47, no. 1, pp. 558-561, 01/01/ 1993, doi: 10.1103/PhysRevB.47.558.
[41] J. P. Perdew *et al.*, "Restoring the Density-Gradient Expansion for Exchange in Solids and Surfaces," *Phys. Rev. Lett.* , vol. 100, no. 13, p. 136406, 04/04/ 2008, doi: 10.1103/PhysRevLett.100.136406.
[42] G. Kresse and D. Joubert, "From ultrasoft pseudopotentials to the projector augmented-wave method," *Phys. Rev. B,* vol. 59, no. 3, pp. 1758-1775, 01/15/ 1999, doi: 10.1103/PhysRevB.59.1758.
[43] V. Wang, N. Xu, J.-C. Liu, G. Tang, W.-T. Geng, "vaspkit,, A user-friendly interface facilitating high-throughput computing and analysis using VASP code,", Comput. Phys. Commun. 267 (2021) 108033 https://doi.org/10.1016/j.cpc.2021.108033.
[44] R.D. Shannon, Revised effective ionic radii and systematic studies of interatomic distances in halides and chalcogenides, Acta Crystallogr. Sect. A: Cryst. Phys., Diffr., Theor. Gen. Crystallogr. 32 (5) (1976) 751–767.
[45] I. Brown, D. Altermatt, Bond-valence parameters obtained from a systematic analysis of the inorganic crystal structure database, Acta Crystallogr. B 41 (4) (1985) 244–247.
[46] N. Brese, M. O'keeffe, Bond-valence parameters for solids, Acta Crystallogr. B 47 (2) (1991) 192–197.
[47] H. Zhang, et al., Antisite defects and Mg doping in LiFePO 4: a first-principles investigation, Appl. Phys. A 104 (2011) 529–537.
[48] H. Li, et al., Effects of Mg doping on the remarkably enhanced electrochemical performance of Na 3 V 2 (PO 4) 3 cathode materials for sodium ion batteries, J. Mater. Chem. A 3 (18) (2015) 9578–9586.
[49] J.Z. Guo, et al., Heterogeneous NASICON-Type Composite as Low-Cost, High-Performance Cathode for Sodium-Ion Batteries, Adv. Funct. Mater. 32 (52) (2022) 2209482.
[50] S. Li, et al., A nanoarchitectured Na 6 Fe 5 (SO 4) 8/CNTs cathode for building a low-cost 3.6 V sodium-ion full battery with superior sodium storage, J. Mater. Chem. A 7 (24) (2019) 14656–14669.
[51] P. Barpanda, G. Oyama, S.-I. Nishimura, S.-C. Chung, A. Yamada, A 3.8-V earth-abundant sodium battery electrode, Nat. Commun. 5 (1) (2014) 4358.
[52] S.-C. Chung, J. Ming, L. Lander, J. Lu, A. Yamada, Rhombohedral NASICON-type Na x Fe 2 (SO 4) 3 for sodium ion batteries: comparison with phosphate and alluaudite phases, J. Mater. Chem. A 6 (9) (2018) 3919–3925.
[53] W. Wang, et al., A high voltage cathode of Na 2+ 2x Fe 2–x (SO 4) 3 intensively protected by nitrogen-doped graphene with improved electrochemical performance of sodium storage, J. Mater. Chem. A 6 (10) (2018) 4354–4364.
[54] W. Niu, et al., Mesoporous N-doped carbons prepared with thermally removable nanoparticle templates: an efficient electrocatalyst for oxygen reduction reaction, J. Am. Chem. Soc. 137 (16) (2015) 5555–5562.
[55] M. Li, H. Du, L. Kuai, K. Huang, Y. Xia, B. Geng, Scalable dry production process of a superior 3D net-like carbon-based iron oxide anode material for lithium-ion batteries, Angew. Chem. Int. Ed. 56 (41) (2017) 12649–12653.
[56] X. Wang, et al., Unlocking fast and highly reversible sodium storage in Fe-based mixed polyanion cathodes for low-cost and high-performance sodium-ion batteries, J. Mater. Chem. A 11 (13) (2023) 6978–6985.
[57] X. Ma, et al., Tuning crystal structure and redox potential of NASICON-type cathodes for sodium-ion batteries, Nano Res. 13 (2020) 3330–3337.
[58] Y. You, et al., "Subzero-temperature cathode for a sodium-ion battery,", Adv. Mater. (Deerfield Beach Fla.) 28 (33) (2016) 7243–7248.
[59] P.-L. Taberna, S. Mitra, P. Poizot, P. Simon, J.-M. Tarascon, High rate capabilities Fe3O4-based Cu nano-architectured electrodes for lithium-ion battery applications, Nat. Mater. 5 (7) (2006) 567–573.
[60] J. Zhang, et al., Understanding the superior sodium-ion storage in a novel Na3. 5Mn0. 5V1. 5 (PO4) 3 cathode, Energy Storage Mater. 23 (2019) 25–34.
[61] F. Cheng, et al., Porous LiMn 2 O 4 nanorods with durable high-rate capability for rechargeable Li-ion batteries, Energ. Environ. Sci. 4 (9) (2011) 3668–3675.
[62] Y. Ma, C. Fang, B. Ding, G. Ji, J.Y. Lee, Fe-doped MnxOy with hierarchical porosity as a high-performance lithium-ion battery anode, Adv. Mater. 25 (33) (2013) 4646–4652.
[63] L. Wang, et al., Electrochemical impedance spectroscopy (EIS) study of LiNi1/3Co1/3Mn1/3O2 for Li-ion batteries, Int. J. Electrochem. Sci. 7 (1) (2012) 345–353.
[64] E. Talaie, P. Bonnick, X. Sun, Q. Pang, X. Liang, L.F. Nazar, Methods and protocols for electrochemical energy storage materials research, Chem. Mater. 29 (1) (2017) 90–105.
[65] R.R. Gaddam, L. Katzenmeier, X. Lamprecht, A.S. Bandarenka, Review on physical impedance models in modern battery research, PCCP 23 (23) (2021) 12926–12944.
[66] A. C. Lazanas and M. I. Prodromidis, "Electrochemical Impedance Spectroscopy— A Tutorial," *ACS Measurement Science Au,* 2023.
[67] H. Liu, C. Li, H. Zhang, L. Fu, Y. Wu, H. Wu, Kinetic study on LiFePO4/C nanocomposites synthesized by solid state technique, J. Power Sources 159 (1) (2006) 717–720.
[68] J. Tian, D. Cao, X. Zhou, J. Hu, M. Huang, C. Li, High-capacity Mg–organic batteries based on nanostructured rhodizonate salts activated by Mg–Li dual-salt electrolyte, ACS Nano 12 (4) (2018) 3424–3435.
[69] Y. Huang, et al., Superior Na-ion storage achieved by Ti substitution in Na3V2 (PO4) 3, Energy Storage Mater. 15 (2018) 108–115.
[70] W. Zheng, et al., GITT studies on oxide cathode LiNi 1/3 Co 1/3 Mn 1/3 O 2 synthesized by citric acid assisted high-energy ball milling, Bull. Mater. Sci. 36 (2013) 495–498.